Research Square

Preprints are preliminary reports that have not undergone peer review.
They should not be considered conclusive, used to inform clinical practice,
or referenced by the media as validated information.

Topology-Resolved Imaging of Mitochondrial Nucleoid Condensates Uncovers Dynamic G-Quadruplex Remodeling

Jong Seung Kim

jongskim@korea.ac.kr

Korea University https://orcid.org/0000-0003-3477-1172

Xin-Ru Hu

Shandong University

Yan Lin

Qilu Hospital of Shandong University

Meng-Di Chen

State Key Laboratory of Crystal Materials, Shandong University

Man Zhang

Shandong University

Eunji Kim

Korea University

Jungryun Kim

Korea University

Fuchen Liu

Qilu Hospital of Shandong University

Kunqian Ji

Qilu Hospital of Shandong University

Zhiqiang Liu

Shandong University

Chuanzhu Yan

Qilu Hospital of Shandong University https://orcid.org/0000-0002-2191-5184

Yunjie Xu

Korea University https://orcid.org/0000-0003-0730-8473

Xiaoqiang Yu

Shandong University

Kang-Nan Wang

State Key Laboratory of Crystal Materials, Shandong University https://orcid.org/0000-0002-0835-8803

Article

Keywords:

Posted Date: April 1st, 2026

DOI: https://doi.org/10.21203/rs.3.rs-9241346/v1

License: This work is licensed under a Creative Commons Attribution 4.0 International License. Read Full License

Additional Declarations: There is **NO** Competing Interest.

Abstract

G-quadruplex structures in mitochondrial DNA (mtG4DNA) have been implicated in mitochondrial genome regulation and cellular metabolism, yet their spatial organization within mitochondrial nucleoids remains poorly understood. A central challenge is that mtG4DNA cannot be readily distinguished from mitochondrial double-stranded DNA (mt-dsDNA) in living cells, which has limited direct analysis of topological remodeling under stress and disease conditions. Here, we report SDMNA, a mitochondria-targeted fluorescent probe that enables topology-resolved imaging of mtDNA in situ. Built on a Y-shaped triphenylamine scaffold, SDMNA generates distinct optical responses to different mtDNA conformations. Binding to G4DNA imposes stronger conformational restriction on the probe, resulting in increased fluorescence intensity and a longer fluorescence lifetime relative to duplex binding. Together with its large Stokes shift and high photostability, these properties support fluorescence lifetime imaging microscopy and STED nanoscopy for quantitative discrimination of mtG4DNA and mt-dsDNA in living cells. Using this approach, we identify condition-dependent remodeling of mitochondrial DNA topology in oxidative stress, replicative senescence, and FUS-mutant amyotrophic lateral sclerosis patient-derived fibroblasts. These findings establish SDMNA as a platform for probing mitochondrial nucleoid organization and mtDNA structural remodeling in aging- and disease-associated mitochondrial dysfunction.

Introduction

Mitochondrial nucleoids are dynamic nucleic acid-protein assemblies in the mitochondrial matrix that organize, protect, and regulate the mitochondrial genome[1-3]. Although mitochondrial DNA (mtDNA) is typically considered in its canonical double-stranded form (mt-dsDNA), it can also adopt non-canonical topologies, including G-quadruplex DNA (mtG4DNA). These alternative topological states are increasingly recognized as functionally relevant features of the mitochondrial genome, with reported roles in replication, transcription, and genome maintenance. Because mtDNA is located close to the electron transport chain and lacks histone protection, it is particularly vulnerable to oxidative stress. Such stress can induce DNA damage, fragmentation, and topological rearrangement, ultimately compromising mitochondrial gene expression, metabolism, and organelle function[4-7]. In line with this, nucleoid topology dysregulation has been linked to metabolic aging, neurodegenerative diseases, and other mitochondria-associated disorders[8-11]. Nevertheless, how distinct mtDNA topologies are spatially organized and dynamically remodeled within nucleoids under physiological and pathological conditions remains poorly understood[12].

Among these topological states, mtG4DNA has emerged as a particularly important structural feature of the mitochondrial genome. Accumulating evidence suggests that mtG4DNA is responsive to redox imbalance and metabolic stress, and may participate in regulating mitochondrial genome transactions[13-17]. Its abundance and structural characteristics have been reported to change during cellular aging and oxidative stress-associated degeneration. Yet direct evidence for mtDNA topological remodeling in

disease-relevant settings remains limited. This issue is especially pertinent in amyotrophic lateral sclerosis (ALS), a fatal neurodegenerative disorder increasingly associated with mitochondrial dysfunction, genome instability and aberrant innate immune activation. Whether ALS is accompanied by spatially resolved remodeling of mtDNA topology, particularly in living cells or patient-derived samples, remains scarce. A major challenge has been the lack of tools capable of distinguishing mtG4DNA from mt-dsDNA while simultaneously preserving the spatial context of native nucleoids.

Fluorescence imaging offers a non-invasive approach to visualize intracellular structures in real time and is well suited for quantitative analysis of nucleic acid content and dynamics within cells. Recent advances in fluorescence microscopy, particularly stimulated emission depletion (STED) imaging and fluorescence lifetime imaging (FLIM), provide new opportunities to interrogate mitochondrial nucleoids with high spatial and temporal resolution[18-23]. FLIM is particularly powerful for quantitative live-cell imaging, as it measures fluorescence lifetime rather than intensity, reducing sensitivity to probe concentration, excitation fluctuations, and optical heterogeneity, while directly reporting local microenvironmental properties[24]. However, the success of these approaches depends critically on the design of imaging tools. An effective tool for topology-resolved nucleoid imaging should selectively accumulate in mtDNA with minimal nuclear interference, remain photostable under intense illumination, exhibit a large Stokes shift, and generate topology-dependent optical responses that distinguish mtG4DNA from mt-dsDNA[25-28].

Existing methods, such as genetic labeling, immunostaining, and fluorescence *in-situ* hybridization, can provide good specificity, but they generally require fixation, genetic manipulation, or endpoint analysis, limiting their utility for monitoring dynamic remodeling in living systems or minimally processed clinical sample[29-33]. Small-molecule fluorescent probes combine high sensitivity, rapid cellular permeability, and tunable targeting, enabling real-time, multicolor, nanoscale imaging of dynamic cellular processes using advanced techniques such as STED and FLIM. However, recently reported conventional DNA dyes[34, 35] stain both nuclear and mitochondrial DNA indiscriminately and provide limited information on DNA topology. Fluorescent probes that can precisely target mtDNA and distinguish mtG4DNA from mt-dsDNA via FLIM are highly attractive, yet their design remains challenging.

Here, we introduce SDMNA, a mitochondrial nucleoid targeted fluorescent probe that enables topology-resolved imaging of mtDNA. Built on a Y-shaped triphenylamine scaffold, SDMNA integrates mitochondrial targeting, DNA binding, and twisted intramolecular charge transfer (TICT) based signal transduction within a single molecular framework. Upon binding mtG4DNA or mt-dsDNA, SDMNA exhibits distinct fluorescence intensity and lifetime signatures, enabling quantitative discrimination of mtDNA topologies in living cells using combined STED and FLIM imaging. Using this platform, we visualize and quantify mtDNA remodeling under oxidative stress models, replicative senescence, revealing condition-dependent, topology-selective reorganization together with a decoupling between mtDNA structural state and overall DNA abundance.

Extending this approach to *FUS*-mutant ALS patient-derived samples, we identify a spatially restricted shift characterized by increased mtG4DNA and reduced mt-dsDNA. This pattern resembles the topology signature observed in metabolic-aging and points to mtDNA structural remodeling as a previously underappreciated feature of ALS-associated mitochondrial dysfunction. In summary, this work presents a fluorescent tool compatible with STED and FLIM for topology-resolved imaging of mitochondrial nucleoids, revealing mtDNA remodeling under oxidative stress, senescence, and ALS, and highlighting topology-selective reorganization as a key feature of mitochondrial genome regulation.

Results and Discussion

Probe design and synthesis. The probe SDMNA was designed on a triphenylamine fluorophore scaffold[36], which provides a Y-shaped molecular framework with high modularity and robust fluorescence emission. Two side arms of the triphenylamine unit were introduced with pyridinium to extend the π-conjugation, enhance electron-accepting character, and promote electrostatic interactions with the negatively charged phosphate backbone of DNA. These pyridinium cationic groups were also expected to promote mitochondrial accumulation. To further modulate amphiphilicity and DNA affinity, a hydroxylated chalcone unit was then installed on the third arm via a classic *Claisen-Schmidt condensation* reaction. This modification increases polarity and introduces hydrogen-bonding capability, both of which are expected to influence probe-DNA interactions. The synthetic route to SDMNA and its key intermediates is shown in Scheme S1. The identity and purity of SDMNA were confirmed by ^{1}H NMR, ^{13}C NMR, and HRMS (Figs. S1-S8).

Photophysical characterization and DNA binding evaluation. SDMNA showed comparable absorption and emission profiles across different solvents (Fig. 1a and Fig. S9), with a high-energy absorption band near ~280 nm and a dominant band near ~440 nm. Upon 440 nm excitation, SDMNA emits near ~630 nm and shows a long red tail extending to ~850 nm, compatible with the 775 nm *p*-STED depletion wavelength commonly used for super-resolution imaging. SDMNA also presents a large Stokes shift of ~200 nm, which is advantageous for minimizing self-absorption and reducing spectral overlap, thereby improving imaging contrast.

Consistent with its rotor-like architecture, SDMNA displays strong viscosity-responsive fluorescence behavior. Increasing the glycerol fraction resulted in up to an 18-fold enhancement in fluorescence intensity, and the emission peak shifted slightly to a shorter wavelength (Fig. 1b). In contrast, SDMNA showed negligible fluorescence variation across a broad pH range (pH 3-10) (Fig. 1c), indicating minimal pH-sensitivity under physiological conditions. In viscous environments, restriction of intramolecular rotation suppresses non-radiative decay pathways and favors radiative recombination, thereby enhancing fluorescence output (Fig. 1d). Additional interference studies with biologically relevant ions and bioactive molecules (Fig. S10) showed little effect on SDMNA emission, supporting the stability of the signal in complex biological environments.

To assess DNA binding behavior under physiologically relevant conditions, fluorescence titration experiments were conducted in 10 mM Tris-HCl buffer (pH: 7.2, 100 mM K^+) using different DNA topologies, including double-stranded DNA (dsDNA), nuclear G4DNA, and mitochondrial G4DNA[37, 38] (Fig. 1e and Fig. S11). Upon binding to DNA, SDMNA presented significant fluorescence enhancement ranging from 2- to 85-fold, depending on different DNA topologies. For representative mtG4DNA sequences (such as mtDNA1015), fluorescence increased by ~55-fold. In contrast, the responses to mt-dsDNA (such as mtDNA15653[39]) and human serum albumin (HSA) were substantially smaller, at ~8-fold and ~6-fold, respectively (Fig. S11). Across the tested sequences, mtG4DNA consistently produced stronger fluorescence enhancement than mt-dsDNA (Fig. S12), indicating a clear preference for G-quadruplex structures.

Time-resolved fluorescence measurements further revealed topology-dependent fluorescence lifetime responses of SDMNA. Upon binding to mtDNA1015, the fluorescence lifetime of SDMNA increases from 1.5 ns to 4.4 ns (Fig. 1f), whereas binding to mtDNA15653 produced a shorter lifetime of 2.9 ns (Fig. 1g). Across all sequences examined, G-quadruplex binding yielded significantly longer fluorescence lifetimes than dsDNA binding (Figs. 1h-i). At saturation, G4DNA gave dominant lifetime distributions of ~3.0-4.5 ns, while dsDNA gave shorter values of ~1.5-2.9 ns (Fig. S13 and Tables S1-S2). These results demonstrate that restriction of intramolecular rotation enables dual-mode discrimination of G4DNA through both fluorescence amplification and lifetime elongation (Fig. 1d). To assess the robustness of lifetime-based detection, the fluorescence lifetime of SDMNA was further evaluated under varying viscosity, pH, and solvent conditions (Fig. S14 and Table S3). Only minor changes were observed, confirming that once bound to G4DNA, the lifetime signal is largely insensitive to environmental fluctuations. This photophysical stability renders SDMNA particularly well suited for accurate fluorescence FLIM-based imaging in living cells.

To gain insight into the molecular basis of topology selectivity, flexible ligand docking was performed using two representative structures: a canonical G-quadruplex (C-MYC, PDB ID: 6JJ0) and an mtDNA-protein complex (PDB ID: 7LBW). Detailed binding energies and conformational analyses are listed in Tables S4-S5, and the most favorable binding poses are shown in Figs. 1j-k. In the case of C-MYC, SDMNA mainly stacks onto the terminal G-quartet and is further stabilized by an adjacent adenine residue. This binding is supported by π-π stacking, electrostatic forces, and hydrogen bonding between the phenolic hydroxyl group of SDMNA and G4DNA bases. In contrast, docking with the mtDNA-protein complex revealed a distinct binding mode. Two pyridinium side arms insert into the duplex minor groove and interact with the phosphate backbone via electrostatic interactions, while the third side arm forms stabilizing hydrogen bonds with adjacent bases (Fig. 1l). Compared with duplex binding, the G4DNA configuration imposes tighter conformational restriction on the probe. Given the TICT character of SDMNA (Fig. 1m), this more constrained environment is expected to suppress non-radiative decay, thereby accounting for the stronger intensity and longer lifetime observed upon G4DNA binding.

Live-cell super-resolution imaging of mitochondrial nucleoids. Encouraged by the strong and selective recognition of G4DNA in solution, we next investigated the intracellular localization and imaging

performance of SDMNA in living cells. COS-7 cells were incubated with SDMNA for 2 h and imaged by STED, with co-staining using the mitochondrial inner membrane dye PKMO[40]. Under 488 nm excitation and 775 nm *p*-STED depletion, SDMNA generated distinct punctate green fluorescence signals within mitochondria (Fig. 2a), which match mitochondrial nucleoid structures in the mitochondrial matrix. Increasing the STED depletion power sharpened these puncta, and the saturation power ($P_{sat.}$) required for 50% fluorescence depletion was 9.28 mW (Fig. S15), supporting the suitability of SDMNA for STED imaging. Magnified regions of interest (ROI) (Fig. 2b-2c) showed SDMNA signals were localized within the mitochondrial cristae, and the morphology and size matched mtDNA labeled by the commercial dye PicoGreen (Fig. S16). PicoGreen stains DNA in both mitochondria and the nucleus, whereas SDMNA selectively labels mtDNA in living cells. STED imaging resolved individual mitochondrial nucleoids with a minimum full width at half maximum (FWHM) of ~110 nm, markedly improving upon the ~290 nm measured by conventional CLSM (Fig. 2d). STED imaging clearly reveals the gaps between the mitochondrial nucleoid and the inner mitochondrial membrane. Notably, mitochondrial nucleoids are not only widely present in filamentous mitochondria but also contain one such nucleoid within granular mitochondria (Fig. 2e).

In addition, SDMNA overlapped strongly with POLG2-mCherry, a red fluorescent marker specifically labeling mitochondrial nucleoids[41], yielding a Pearson correlation coefficient (PCC) of 0.83 (Fig. 2f), consistent with its selective labeling of mitochondrial nucleoids. To exclude nonspecific staining, cells were co-stained with the lysosomal probe LysoTracker Deep Red and the lipid droplet dye PDM[42], both of which presented minimal overlap with SDMNA (Fig. S17), further supporting its preferential labeling of mitochondrial nucleoids. SDMNA exhibited superior photostability compared with PicoGreen and homo-POLG2-mCherry (Fig. 2g), maintained >80% cell viability across four cell lines (HeLa, COS-7, U2OS, and MCF-10A) at 0.5-15 μM (Fig. S18), and did not alter basal or ATP-linked respiration, proton leak, or maximal oxygen consumption rates, supporting its suitability for long-term imaging of mitochondrial nucleoids (Fig. 2h and Fig. S19).

To evaluate whether the probe's ability to image mitochondrial nucleoids was cell-type dependent, STED imaging was repeated in U2OS and MCF-10A cells under identical settings (Figs. 2i-2j and Fig. S20). Distinct nucleoid morphologies were apparent between the two cell types: U2OS cells tended to display smaller mitochondrial nucleoids, whereas MCF-10A cells displayed larger structures. PKMO co-staining further revealed differences in mitochondrial ultrastructure, mitochondria in U2OS cells appeared elongated with relatively sparse cristae, while those in MCF-10A cells were thicker and characterized by denser cristae, consistent with reported metabolic differences between these lines[43]. Beyond STED imaging, SDMNA is also compatible with 3D ultrafast structured illumination microscopy (3D-SIM)[44, 45]. In COS-7 cells co-stained with SDMNA and MitoTracker Deep Red (MTDR), nucleoids were distributed throughout the mitochondrial network (Figs. 2k-l). Subsequent 3D reconstruction using the Imaris software showed that mtDNA is distributed unevenly within the mitochondrial matrix (Fig. 2m). Time-lapse imaging (Movie S1 and Fig. S21) captured rapid nucleoid motion and frequent interactions. In ROI 1, we observed a division event over 10 frames (2 s per frame),

while in another region (ROI 2), we saw brief contacts between neighboring nucleoids resembling a “kiss-and-run” behavior (Fig. S21). Together, these results establish SDMNA as a versatile probe for super-resolution and long-term live-cell imaging of mitochondrial nucleoid organization and dynamics.

Fluorescence lifetime analysis of mitochondrial nucleoids in living cells. FLIM provides concentration-independent contrast and is therefore well suited for quantitative live-cell imaging. Given the distinct lifetime response of SDMNA toward G4DNA and dsDNA in solution, we next applied the probe to FLIM imaging of mitochondrial nucleoids in living cells. Photon-count intensity maps and corresponding fluorescence lifetime distributions are shown in Figs. 3a-3c. In ROI 1, two mitochondrial nucleoids (ROI 3 and ROI 4) were randomly selected for detailed analysis (Fig. 3b). In both mitochondrial nucleoids, the photon signal was strongest at the center, and when two nucleoids that were closely apposed, the line profile still resolved a clear “double-peak” structure. Quantitative analysis of the FLIM data from ROI 1 (Fig. 3c) revealed that the overall lifetime distribution (Fig. 3d) closely matched the lifetime ranges obtained for SDMNA interacting with different DNA structures in solution.

Fluorescence lifetime mapping reported heterogeneity of mitochondrial nucleoids that was not evident from fluorescence intensity alone. In the zoomed ROI 5 from Fig. 3c, lifetimes varied across a single nucleoid even though the photon counts were relatively even (Fig. 3e). Four points (#1-4) were selected for analysis (Fig. 3f). Point #1 presented a fluorescence lifetime of 3.12 ns, consistent with the G4DNA-bound state measured in solution. Points #2 and #3 presented 2.83 ns and 1.78 ns, respectively, which are closer to the dsDNA-associated range. The nearby background (point #4) showed a very short lifetime (0.11 ns), consistent with a nonspecific signal. Using the solution calibration, we grouped the cellular lifetimes into ranges (Fig. 3g-3i): ≥3.0 ns for G4DNA-bound SDMNA, 2.0-3.0 ns for dsDNA binding, and ≤2.0 ns for other contributions, such as other proteins or fragmented DNA. Quantification of the signal fraction within each bin (Fig. 3j) provided a practical framework for estimating the relative abundance of mtG4DNA level in living cells.

FLIM imaging and metabolic profiling of mitochondrial G4DNA in senescence models. Oxidative stress and aging impose sustained damage on mitochondria and are commonly accompanied by mitochondrial dysfunction, DNA lesions, and altered mitochondrial homeostasis [46, 47]. Because nucleoid-associated proteins provide only limited protection, mtDNA is highly susceptible to oxidative injury, which can lead to mutation, fragmentation, and copy number alterations. Although mtG4DNA has been implicated in regulating mtDNA replication, transcription, and stability, its behavior in different senescence contexts remains incompletely understood. To address this challenge, we applied the SDMNA-FLIM imaging platform to two senescence models: (i) an acute senescence model generated by H_2O_2 treatment in MCF-10A cells (Figs. 4a-4d), and (ii) a replicative senescence model established by serial passaging of C2C12 myoblasts (Figs. 4e-4h). Both models were confirmed using Western blot analysis and Seahorse-based metabolic profiling.

In the H_2O_2-induced oxidative stress model, senescence markers P21 and P53 were markedly upregulated (Fig. S24). Senescence-associated β-galactosidase staining revealed characteristic

phenotypic changes, including enlarged cell size, irregular morphology, and strong *β*-galactosidase positivity (Fig. S26). The expression of several OXPHOS complexes' subunits was reduced, such as NDUFB8 (complex I), SDHB (complex II), UQCRC2 (complex III), CO2 (complex IV), and ATP5A (complex V) (Fig. S27). Seahorse profiling showed broad respiratory defects, with lower basal respiration, ATP-linked respiration, maximal respiratory capacity, and spare respiratory capacity, along with decreased proton leak, while non-mitochondrial respiration remained largely unchanged (Fig. S28). These results confirm the onset of oxidative stress-associated senescence.

FLIM imaging showed that untreated MCF-10A cells exhibited abundant long-lifetime fluorescence signals (2.0-3.0 ns and ≥3.0 ns), indicative of intact mtDNA and structured G4DNA (Figs. 4a-4b). In contrast, H_2O_2-treated cells displayed a marked loss of long-lifetime signals and a concomitant increase in short-lifetime components (1.0-2.0 ns) (Figs .4c-4d), consistent with more disordered or fragmented mtDNA. A side-by-side comparison of the signal proportions within the same fluorescence lifetime range between the H_2O_2 group and control group indicates that fluorescence lifetime distributions showed a significant decrease in the > 3 ns population (Fig. 4i), while the proportion of 2-3 ns signals rose slightly (Fig. S22). To assess whether these structural alterations were accompanied by changes in mtG4DNA abundance, mitochondria were isolated and mtDNA was quantified by qPCR using primers targeting G4-prone regions. Under acute oxidative stress, mtDNA content was reduced (Fig. 4j), supporting an overall loss of mtDNA, including G4-enriched regions, during ROS exposure.

Replicative senescence in C2C12 cells showed a different pattern. Cells passaged 18 times or more are defined as late-passage cells (P18), while cells passaged 2 times are defined as young-passage cells (P2). Late-passage cells (P18) had higher expression of p21 and p53 (Fig. S25) and strong SA-*β*-gal staining (Fig. S26) compared to early-passage (P2) cells. OXPHOS protein levels were largely stable (complexes I-IV) and complex V changed little (Fig. S27), while Seahorse analysis still showed reduced basal respiration, ATP production, maximal respiration, spare respiratory capacity, and proton leak in P18 cells (Fig. S29), consistent with a senescent phenotype. FLIM imaging showed a modest but reproducible increase in long-lifetime fluorescence signals in senescent P18 cells compared to young P2 cells (Fig. 4e-4h). Unlike the oxidative stress model, replicative senescence did not produce a prominent accumulation of short-lifetime components (Fig. S23). Instead, the ≥3.0 ns fraction increased slightly in P18 cells (Fig. 4k), suggesting gradual enrichment or stabilization of structured mtG4DNA rather than widespread mtDNA fragmentation. qPCR analysis also showed increased copy numbers of G4-prone mtDNA regions in P18 cells (Fig. 4l), consistent with compensatory amplification of mtDNA during senescence. Together, these findings distinguish the two senescence states (Fig. 4m): acute oxidative stress is associated with mtDNA loss and disruption of mtG4DNA, while replicative senescence is accompanied by topology remodeling with preserved, or even increased, G4-prone mtDNA content.

Mitochondrial G4DNA perturbation and mitochondrial dysfunction in ALS samples with *FUS* mutations. ALS pathogenesis is closely linked to mitochondrial dysfunction, oxidative stress, and dysregulated nucleic acid metabolism[48]. Among ALS-linked genes, *FUS* represents a major pathogenic factor; disease-associated mutations in *FUS* can disrupt mitochondrial homeostasis and DNA repair, thereby

accelerating neurodegeneration[49, 50]. Despite these links, the effect of *FUS* mutations on mtDNA topology, and particularly on mtG4DNA, remain poorly defined. To address this question, we analyzed samples from ALS patients carrying *FUS* mutations together with age-matched healthy male controls. Sanger sequencing verified the presence of the *FUS* c.1574C>T (p.P525L) mutation in patient muscle tissue (Fig. 5a). Under physiological conditions, FUS mainly localizes in the nucleus. In ALS, however, mutant *FUS* aberrantly accumulates in the cytoplasm, forms aggregates and establishes pathological interactions with mitochondria, which is thought to damage mitochondrial function[51-53]. In line with this model, immunofluorescence analysis revealed increased FUS protein associated with mitochondria in patient samples (Fig. 5b). Western blot analysis (Fig. 5c) and tissue section staining (Fig. S30) further showed abnormal expression of mutant FUS and reduced levels of respiratory-chain components, with the largest decreases incomplexes I and IV (Fig. 5e). To corroborate these findings in a cellular model, a primary fibroblast cell line was subsequently established from the patient's skin biopsy (Fig. 5d). Patient-derived fibroblasts showed the same trend of respiratory complex suppression (Fig. 5e). Seahorse analysis indicated lower basal respiration, ATP-linked respiration, maximal respiratory capacity, and spare respiratory capacity (Fig. S31). Consistent with these results, JC-1 staining and DCFH-DA flow cytometry analysis revealed decreased mitochondrial membrane potential (Fig. S32) and elevated ROS levels (Fig. S33).

We next used the SDMNA-FLIM platform to examine mtDNA topology directly. In healthy controls, SDMNA lifetimes were concentrated in the 2.0-3.0 ns range (consistent with mt-dsDNA) and included a distinct population above 3.0 ns, indicative of mtG4DNA structure (Figs. 5f-5g). In *FUS*-mutant ALS samples, short-lifetime signals (1.0-2.0 ns) increased, while the 2.0-3.0 ns fraction decreased modestly (Fig. 5h-5i, and Fig. S34), which points to partial disruption of mtDNA structure. qPCR analysis further demonstrated a significant reduction in total mtDNA copy number in patient-derived fibroblast (Fig. S35). Notably, however, the ≥3.0 ns lifetime fraction rose slightly (Fig. 5j), suggesting localized accumulation or stabilization of mtG4DNA despite the overall loss of mtDNA. This interpretation was supported by qPCR analysis of G4-prone mtDNA regions, which showed higher copy numbers in patient samples (Fig. 5k). Together, these findings indicate a composite phenotype characterized by global mtDNA loss together with relative mtG4DNA enrichment, consistent with chronic oxidative stress and impaired mitochondrial maintenance (Fig. 5l). Collectively, these findings indicate that *FUS* mutations are associated with substantial remodeling of mitochondrial DNA topology rather than a simple uniform loss of mtDNA. By combining topology-sensitive fluorescence readouts with FLIM, SDMNA enabled direct visualization of shifts in both mtDNA structural state and mtG4DNA-associated signals in patient-derived samples. The probe maintained clear lifetime separation under disease-relevant conditions, highlighting its utility as a chemical tool for probing mitochondrial genome organization and G-quadruplex remodeling in neurodegenerative disease contexts.

Discussion

mtG4DNA within mitochondrial nucleoids is increasingly recognized as a structurally and functionally relevant feature of the mitochondrial genome, with potential consequences for mitochondrial gene expression, bioenergetics regulation, and neurological disease. However, direct discrimination of mtG4DNA from mt-dsDNA in living cells remains difficult. Most available imaging methods primarily report nucleoid abundance or total DNA content rather than DNA topology, and only a limited number of approaches provide quantitative, spatially resolved information on distinct mtDNA structural states. As a result, direct analysis of topology remodeling during oxidative stress, cellular senescence, and disease progression has remained limited.

Existing strategies only addressed part of this problem[54]. Conventional dsDNA dyes, such as PicoGreen, are useful for visualizing mitochondrial nucleoids, but they mainly report the abundance of dsDNA, show substantial nuclear background, and do not distinguish DNA topology[55]. Antibody-based approaches such as BG4 provide high specificity for intracellular G-quadruplexes, but generally require fixation and are dominated by nuclear G4 signals, which limits their use for live-cell analysis of mtDNA[56]. Small molecule ligands, including MitoISCH[57], thioflavone T[58], and more recently Ir2PDP[59], have broadened the chemical toolkit for G4 recognition, but most do not combine mitochondrial selectivity, super-resolution compatibility, and quantitative discrimination of topological states within intact nucleoids. Against this background, SDMNA fills an important methodological gap by enabling intranucleoid topological heterogeneity to be resolved directly in living cells, allowing mtG4DNA- and mt-dsDNA-associated signals to be distinguished rather than inferred indirectly.

This capability arises from the topology-dependent photophysics of SDMNA. By integrating mitochondrial targeting, nucleic-acid binding, and TICT-based signal transduction within a Y-shaped triphenylamine scaffold, SDMNA converts differences in mtDNA topology into separable optical outputs. Binding to G4DNA is expected to impose stronger conformational restriction on the probe than duplex binding, thereby favoring a more emissive state with higher fluorescence intensity and a longer fluorescence lifetime. In practice, this produces distinct intensity-lifetime signatures for mtG4DNA and mt-dsDNA, providing a workable framework for estimating their relative distribution within mitochondrial nucleoids. The large Stokes shift and favorable photostability of SDMNA further support its use in FLIM and STED imaging under the illumination conditions required for super-resolution analysis.

Using this platform, we found that mtDNA topology is remodeled in a condition-dependent manner that is not apparent from bulk DNA staining alone. In the acute oxidative stress model, SDMNA-FLIM revealed depletion of long-lifetime components together with enrichment of shorter-lifetime signals, consistent with disruption of structured mtDNA and an overall decline in mtDNA integrity. By contrast, replicative senescence produced a different signature, characterized by a relative increase in the long-lifetime fraction associated with mtG4DNA and without the prominent accumulation of short-lifetime signals observed after acute ROS exposure. These findings suggest that stress-associated mitochondrial states are not equivalent at the level of DNA topology. Acute oxidative injury appears to be accompanied by broad structural disruption, whereas replicative senescence is associated with a more gradual

topological reorganization. Importantly, such differences would have been difficult to resolve using conventional mtDNA stains, which primarily reflect DNA abundance rather than structural state.

Our results also extend topology analysis of mtDNAto a disease-relevant setting. Altered G-quadruplex biology has increasingly been implicated in neurodegenerative disorders such as ALS, but direct evidence at the level of mtDNA architecture has remained limited. In *FUS*-mutant ALS patient-derived fibroblasts, SDMNA detected a shift characterized by reduced mt-dsDNA-associated signal together with a modest increase in the mtG4DNA-associated fraction in spatially restricted regions. This pattern partially resembled the signature observed in replicative senescence, raising the possibility that chronic mitochondrial stress in ALS is accompanied by selective enrichment or stabilization of G4-prone mtDNA structures despite an overall reduction in mtDNA content. Although the mechanistic relationship between *FUS* dysfunction, mtG4DNA remodeling, and mitochondrial failure remains to be established, these observations provide direct imaging-based evidence that mtDNA topology is altered in an ALS-relevant context.

Taken together, these findings show that mitochondrial nucleoids are not topologically uniform entities, but structurally dynamic condensates whose DNA organization changes across stress, senescence, and disease states. By enabling topology-resolved imaging of these changes in living cells and patient-derived samples, SDMNA expands the current toolkit for studying mitochondrial genome regulation and offers a framework for investigating how mtDNA structural remodeling contributes to mitochondrial dysfunction.

Methods

Material and Instrumentation

All commercially available reagents and solvents were utilized without further treatment unless otherwise indicated. 4-(diphenylamino)benzaldehyde, N-Bromosuccinimide (NBS), pyridin-4-ylboronic acid, 1-(2-hydroxyphenyl)ethan-1-one, and H_2O_2 were purchased from Bide Pharmatech Ltd. Pyrrolidine and Potassium Hydroxide were purchased from Shanghai Titan Scientific Co. Tetrakis(triphenylphosphine)palladium, tetrahydropyrrole, and K_2CO_3 were purchased from Beijing Inno Chem Science & Technology Co., Ltd. Lyso-Tracker Deep Red (LTDR), Mito Tracker Deep Red (MTDR), and Hoechst 33342 were purchased from Beyotime Biotechnology. PK Mito Orange (PKMO) purchased from Genvivo Biotech. MTT (3-(4, 5-Dimethylthiazol-2-yl)-2, 5-diphenyltetrazolium bromide) was obtained from Sigma Aldrich. The POLG2-mCherry plasmid was purchased from Weizhen Biosciences Ins (Shandong, PR China). Chromatographically pure grade solvents were used to test the spectra, analytically pure solvents were used for the synthesis experiments, and ultrapure water was used for the experiments. Human Serum Albumin (HSA, Sigma-Aldrich) and Bovine Serum Albumin (BSA, Sigma-Aldrich) were purchased from Energy Chemical. Phosphate buffer solution (PBS) and trishydroxymethyl aminoethane (Tris) were purchased from a reagent vendor and sterilized. DNA oligonucleotides were custom-synthesized by Sangon Biotech. Genomic DNA was extracted from peripheral blood using the Blood DNA

Kit V2 (CWBIO, CW2553). Mitochondria were isolated using the Mitochondrial Isolation and Protein Extraction Kit (Proteintech, Cat# PK10016). Mitochondrial DNA was extracted from the mitochondrial pellet using the Tiananpu Genomic DNA Kit (Tiananpu, Catalog No. DP304). Quantitative real-time PCR (qPCR) was performed on a QuantStudio 3 Real-Time PCR System (Thermo Fisher Scientific, Cat# A28567) with ChamQ Universal SYBR qPCR Master Mix (Vazyme, Cat# Q712-02/03). Intracellular ATP levels were measured using a luminescence-based ATP assay kit (Beyotime, S0027). Cellular senescence was assessed using a senescence-associated *β*-galactosidase (SA-*β*-gal) staining kit (Beyotime, Cat# C0602). Materials for Western Blotting, immunohistochemistry, ROS measurements, and mitochondrial membrane potential (MMP) assays are described in the Supplementary Information.

NMR spectra (^{1}H NMR, ^{13}C NMR) and HRMS spectra were collected on a Bruker Avance 400 spectrometer and an Agilent Technologies 6510 Q-TOF LC/MS, respectively. NMR samples were prepared in DMSO-d_6 or Chloroform-*d* with tetramethylsilane (TMS) as the internal chemical shift reference. UV-vis absorption spectra and fluorescence spectra were recorded on a Hitachi U-2910 spectrophotometer and a HORIBA FluoroMax-4 spectrofluorimeter, respectively. Fluorescence lifetime measurements were performed with an Edinburgh Instruments FLS-980 spectrometer. Spectroscopic measurements were performed in quartz cuvettes (1 × 1 cm) with light transmission on all sides. DNA concentration and purity were measured using a NanoDrop spectrophotometer (ND-2000C, Thermo Fisher Scientific). Mitochondrial respiration was assessed using a Seahorse XFe24 extracellular flux analyzer (Agilent Technologies, USA). Confocal fluorescence imaging was obtained using an Olympus FV-1200 microscope or a Leica confocal laser scanning microscope (Germany), as specified in each experiment. STED fluorescence imaging was obtained with an Abberior STEDYCON microscope. SIM fluorescence imaging was obtained with a Multi-SIM ARX. FLIM imaging was obtained from an Abberior STEDYCON system equipped with a time-correlated single-photon counting (TCSPC) module (Becker & Hickl GmbH, Berlin, Germany).

Synthesis

Intermediates S1 and S2 were synthesized following previously reported procedures[36].

4-[Bis(4-bromophenyl)amino]benzaldehyde (**S1**): 4-(Diphenylamino)benzaldehyde (4.10 g, 15 mmol) was placed in a three-necked flask and dissolved in tetrahydrofuran (THF, 40 mL) under nitrogen protection. N-Bromosuccinimide (6.945 g, 39 mmol) was introduced portionwise in six batches at room temperature, and the reaction mixture was stirred for 1.5 h. The mixture was then heated under reflux at 68 °C for 10 h. Upon cooling to ambient temperature, purification was carried out by column chromatography with ethyl acetate/n-hexane (1:300-1:6, v/v) as the mobile phase. S1 was obtained as a pure bright yellow solid (3.9 g) with an isolated yield of 61%. ^{1}H NMR (400 MHz, DMSO-d_6) δ 9.82 (s, 1H), 7.79 - 7.75 (m, 2H), 7.60 - 7.56 (m, 4H), 7.14 - 7.09 (m, 4H), 7.02 - 6.98 (m, 2H).

4-[*Bis*[4-(4-pyridinyl) phenyl] amino] benzaldehyde (**S2**): Compound S1 (1.28 g, 3.0 mmol), pyridin-4-ylboronic acid (1.11 g, 9.0 mmol), and K_2CO_3 (1.24 g, 9.0 mmol) were combined in 1,4-dioxane (15 mL) in

a Schlenk flask under a nitrogen atmosphere. Following the addition of $Pd(PPh_3)_4$ (60 mg), the reaction was allowed to proceed at reflux (110 °C) for 36 h. After the reaction mixture had cooled to room temperature, the crude product was purified by column chromatography using methanol/dichloromethane (1:200 to 1:10, v/v) as the eluent, affording S2 (yellow solid, 1.59 g, 41% yield). ^{1}H NMR (400 MHz, Chloroform-*d*) δ 9.89 (s, 1H), 8.70 - 8.65 (m, 4H), 7.80 - 7.75 (m, 2H), 7.67 - 7.61 (m, 4H), 7.53 - 7.49 (m, 4H), 7.32 - 7.27 (m, 4H), 7.22 - 7.17 (m, 2H).

(*E*)-3-(4-(bis (4-(pyridin-4-yl) phenyl) amino) phenyl)-1-(2-hydroxyphenyl) prop-2-en-1-one (**S3**): 1-(2-Hydroxyphenyl)ethan-1-one (432 μL, 3.6 mmol) was first dissolved in ethanol (15 mL), and S2 (1.28 g, 3.0 mmol) together with pyrrolidine (200 μL) was then introduced into the reaction mixture. Upon stirring at room temperature for 48 h, the reaction produced an orange precipitate. The resulting solid was isolated by filtration and further purified by column chromatography using methanol/dichloromethane (1:100 to 1:2, v/v) as the eluent, affording S3 as an orange solid (0.50 g, 31% yield). ^{1}H NMR (400 MHz, DMSO-d_6) δ 12.66 (s, 1H), 8.64 - 8.60 (m, 4H), 8.24 (dd, *J* = 8.4, 1.7 Hz, 1H), 7.92 (s, 1H), 7.91 - 7.87 (m, 2H), 7.87 - 7.81 (m, 5H), 7.73 - 7.69 (m, 4H), 7.56 (ddd, *J* = 8.6, 7.1, 1.6 Hz, 1H), 7.29 - 7.23 (m, 4H), 7.16 - 7.11 (m, 2H), 7.03 - 6.98 (m, 2H). ^{13}C NMR (101 MHz, DMSO-d_6) δ 193.87, 192.13, 162.38, 150.72, 150.68, 149.39, 147.50, 146.67, 146.56, 144.90, 136.66, 132.95, 131.90, 131.42, 131.18, 129.52, 128.85, 128.74, 128.57, 125.53, 125.29, 124.33, 123.36, 121.27, 121.21, 121.09, 120.30, 119.60, 118.52, 118.22. HRMS: calculated for $C_{37}H_{27}N_3O_2$ $[M+H]^+$: 546.2103 (m/z), found 546.2173.

(*E*)-4,4'-(((4-(3-(2-hydroxyphenyl)-3-oxoprop-1-en-1-yl)phenyl)azanediyl)bis(4,1-phenylene))bis(1-methylpyridin-1-ium) (**SDMNA**): S3 (0.21 g, 0.38 mmol) was allowed to react with iodomethane (53 μL, 0.84 mmol) in acetonitrile (5 mL) at 85 °C for 24 h. After evaporation of the solvent, the residue was washed with methanol. The resulting solid was subsequently dissolved in methanol (5 mL), followed by the addition of NH_4PF_6 (1.30 g, 8.0 mmol). The mixture was stirred at 60 °C for 10 h afford SDMNA as an orange solid (140 mg, 64% yield). ^{1}H NMR (400 MHz, DMSO-d_6) δ 12.54 (s, 1H), 8.95 (d, *J* = 6.7 Hz, 4H), 8.49 - 8.43 (m, 4H), 8.24 (dd, *J* = 8.3, 1.7 Hz, 1H), 8.16 - 8.10 (m, 4H), 8.04 - 7.96 (m, 3H), 7.87 (d, *J* = 15.4 Hz, 1H), 7.58 (ddd, *J* = 8.6, 7.2, 1.7 Hz, 1H), 7.36 - 7.30 (m, 4H), 7.28 - 7.24 (m, 2H), 7.05 - 6.99 (m, 2H), 4.31 (s, 6H). ^{13}C NMR (101 MHz, DMSO-d_6) δ 193.92, 162.33, 153.56, 149.70, 148.16, 145.87, 144.41, 136.81, 131.57, 131.25, 130.26, 128.74, 125.79, 124.84, 123.61, 121.60, 121.29, 119.67, 118.25, 47.35. HRMS: calculated for $C_{39}H_{33}N_3O_2^{2+}$ $[M]^{2+}$:287.6281(m/z), found: 287.6280.

DNA Sample Preparation

DNA sequences are listed in Table S6. Oligonucleotides were dissolved in annealing buffer consisting of 10 mM Tris (pH 7.5-8.0), 50 mM NaCl, and 1 mM EDTA, followed by heating at 95 °C for 5 min and gradual cooling to room temperature to afford the annealed stock solution.

Absorption and Fluorescence Measurements

Unless otherwise noted, spectroscopic measurements were performed using PBS or organic solvents as received. For solvent-dependent studies, probe solutions (5 μM) were prepared in tetrahydrofuran (THF), ethanol (EtOH), ethyl acetate (EA), acetonitrile (MeCN), dimethyl sulfoxide (DMSO), and water (H_2O), and the corresponding absorption/emission spectra were recorded. For the pH response experiment, probe solutions (5 μM) were prepared in Britton-Robinson (BR) buffer with pH adjusted from 3.0 to 10.0 using HCl or NaOH. Fluorescence intensity ratios were recorded after mixing. For viscosity-dependent experiments, solvent viscosity was tuned by varying the glycerol/methanol ratio, followed by probe addition and emission collection. For ion/interference studies, 50 mM stock solutions of common salts and biomolecules were prepared in ultrapure water; final concentrations were 5 μM (probe) and 50 μM (analyte). Samples were mixed thoroughly prior to fluorescence measurements. For DNA titration studies, the annealed DNA was diluted with 10 mM Tris-HCl buffer and mixed with SDMNA (final probe concentration: 1 μM) before recording spectra. For fluorescence lifetime experiments, the probe concentration was 1 μM.

Cell Culture

COS-7 (SV40-transformed renal fibroblasts from African green monkeys), U2OS (human osteosarcoma cells), and C2C12 myoblasts (ATCC) were maintained in DMEM containing 10% fetal bovine serum and 1% penicillin-streptomycin. MCF-10A (human normal mammary epithelial cells) are maintained in MCF-10A Cell Complete Medium. Primary dermal fibroblasts were obtained from a skin biopsy of a patient with the *FUS* c.1574C>T (p.P525L) mutation. Tissue samples were incubated with 0.1% collagenase type I (Gibco) in PBS for 1 h at 37 °C, then subjected to filtration and centrifugation, and finally resuspended in DMEM supplemented with 15% fetal bovine serum and 1% penicillin-streptomycin. Cells were maintained under standard culture conditions and used within 10 passages.

Cellular Cytotoxicity Assay

The MTT assay was employed to determine cell viability. COS-7, HeLa, U2OS, and MCF-10A cells were first seeded in 96-well plates, followed by incubation for 24 h. The cells were subsequently exposed to different concentrations of SDMNA for a further 24 h. MTT solution (20 μL, 5 mg mL^{-1}) was then added to each well, followed by incubation for 4 h. After the medium had been discarded, 100 μL of DMSO was introduced to each well to solubilize the formazan crystals. Using a microplate reader, absorbance was measured at 620 nm, and the percentage of cell viability was calculated according to the formula below:

$$\text{Viability} = (A_{\text{Sample}} - A_{\text{Blank}}) / (A_{\text{DMSO}} - A_{\text{Blank}})$$

Where A_{Sample} is the absorbance of the well with SDMNA, A_{Blank} is the absorbance of the control well with medium only, and A_{DMSO} is the absorbance after DMSO treatment.

Cellular Senescence Models

For oxidative stress-induced senescence, MCF-10A cells were passaged at a 10:1 ratio and maintained under serum-free conditions for 18-20 h. After treatment with H_2O_2 (150 μM) for 1 h, the medium was exchanged for complete MCF-10A medium, and the cells were maintained for approximately 4 days before imaging or collection. For replicative senescence, C2C12 cells at passages 3-10 were classified as "young" whereas cells at passages ≥15 were classified as "aged", based on morphological changes and *β*-galactosidase staining.

Cellular Imaging and Staining

For live-cell imaging, SDMNA was used at 2 μM. To prepare the staining solution, 1 μL of a 2 mM stock solution in DMSO was diluted with 1 mL of culture medium for live cells. The cells were treated with SDMNA at 37 °C for 1.5 h, rinsed two or three times with PBS, and then imaged. Confocal, STED, and FLIM imaging were performed using an Abberior STEDYCON system.SIM time-lapse imaging and 3D SIM datasets were captured on a Multi-SIM ARX system. Data processing was done using ImageJ; plot profiles were generated with GraphPad. STED nanoscopy images were processed by deconvolution with Huygens software (Scientific Volume Imaging B.V., Hilversum, The Netherlands), and SIM images were 3D reconstructed using Imaris software.

For three-color co-staining with SDMNA, PKMO, and Hoechst 33342, the excitation and emission conditions were as follows: $\lambda_{ex/em}$ = 488 nm/505-550 nm for SDMNA (green); $\lambda_{ex/em}$ = 561 nm/650-700 nm for PKMO (red); $\lambda_{ex/em}$ = 405 nm/420-475 nm for Hoechst 33342 (blue). For two-color co-staining with SDMNA and homo-POLG2-mCherry, $\lambda_{ex/em}$ = 488 nm/505-550 nm for SDMNA (green) and $\lambda_{ex/em}$ = 561 nm/650-700 nm for mCherry (red). For three-color co-staining with SDMNA, MTDR, and Hoechst 33342, $\lambda_{ex/em}$ = 488 nm/500-550 nm for SDMNA (green); $\lambda_{ex/em}$ = 640 nm/650-750 nm for MTDR (red); $\lambda_{ex/em}$ = 405 nm/425-475 nm for Hoechst 33342 (blue). Fluorescence lifetime imaging with SDMNA used λ_{ex} = 488 nm and λ_{em} = 575-625 nm.

Molecular Docking

Nucleic acid preparation: DNA structures for mitochondrial DNA (PDB ID: 7lbw) and C-MYC-G4DNA (PDB ID: 6jj0) were obtained from the RCSB Protein Data Bank. SDMNA ligand preparation: SDMNA geometry was optimized through DFT calculations using Gaussian09[60] at the B3LYP/6-31G(d,p) level. RESP was derived from[61] HF/6-31G* calculations. Docking was performed with AutoDock 4.2.6[62] using full ligand flexibility. The Lamarckian genetic algorithm[63]was used with ga_run = 100 and ga_num_evals = 25,000,000; other parameters were default. Complexes were visualized in PyMOL[64].

Plasmid Transfection

COS-7 cells were cultivated in confocal dishes and transitioned to an Opti-MEM culture medium at ~80% confluence. Plasmid DNA (1 μg) and Lipofectamine 2000 (3 μL) were separately diluted in 200 μL Opti-MEM for 5 min, then the Lipofectamine solution was added to the plasmid solution and incubated for 20

min before addition to the cells for 5 h. The medium was then changed to DMEM containing 10% FBS and 1% penicillin-streptomycin, followed by a 24 h incubation before imaging.

Senescence-Associated β-Galactosidase (SA-β-gal) Staining

After washing with PBS, the cells were fixed at room temperature for 15 min and then stained overnight at 37 °C in a CO_2-free incubator using SA-*β*-gal staining solution containing X-gal at pH 6.0. Cells exhibiting blue cytoplasmic staining were classified as senescent, and at least five randomly selected fields were analyzed for each sample.

Western Blot Analysis

Cells and skeletal muscle tissues were lysed for protein extraction and subsequent immunoblot analysis. Muscle tissues were lysed in ice-cold buffer (50 mM Tris-HCl, 150 mM NaCl, 1% NP-40, 0.5% sodium deoxycholate, and 1 mM EDTA) supplemented with protease and phosphatase inhibitors, followed by rotation at 4 °C for 1 h and centrifugation at 12,000 ×g for 15 min. Cultured cells were lysed with RIPA buffer containing the same inhibitors. Protein concentrations were measured using the BCA Protein Assay Kit. Equal amounts of protein were resolved by SDS-PAGE and transferred onto PVDF membranes. After blocking with 5% non-fat milk in TBST for 1 h at room temperature, the membranes were incubated overnight at 4 °C with primary antibodies against Total OXPHOS (Abcam, Cat# ab110413), OXPHOS (Proteintech, Cat# PK30006), FUS (Proteintech, Cat# 11570-1-AP), mitochondria marker (Abcam, Cat# ab92824), VDAC1 (Proteintech, Cat# 55259-1-AP), P21 (Abclonal, Cat# A22460PM), P53 (Abclonal, Cat# A26037PM), P16 (Abclonal, Cat# A11651), *β*-Actin (Proteintech, Cat# 66009-1-Ig), and GAPDH (HUABIO, Cat# EM1101).

Measurement of Intracellular ROS levels

Intracellular ROS was quantified by flow cytometry using DCFH-DA. Cells were resuspended in PBS at 1 × 10^6 cells mL^{-1}, stained with 5 μM DCFH-DA at 37 °C for 15 min in the dark, washed twice with PBS, and immediately analyzed on a BD flow cytometer (E_x/E_m = 488/525 nm). FlowJo was used for data analysis, and mean fluorescence intensity was taken as an indicator of relative ROS levels.

Assessment of Mitochondrial Membrane Potential

MMP was assessed using a JC-1 assay kit following the manufacturer's instructions. Cells (1 × 10^6 cells mL^{-1}) were incubated with JC-1 (10 μg mL^{-1}) for 20 min at 37 °C in 5% CO_2, washed twice, and analyzed by flow cytometry. Fluorescence from JC-1 monomers and aggregates was recorded at 488/530 nm and 525/590 nm, respectively, and MMP was expressed as the red-to-green fluorescence ratio. FCCP (10 μM) served as a positive control.

Genetic Analysis and Variant Detection

Genomic DNA was extracted from peripheral blood with the Blood DNA Kit V2 following the manufacturer's protocol. Libraries were prepared for sequencing on the Illumina NovaSeq platform. Reads were aligned to the GRCh37/hg19 reference genome using BWA-MEM, and variants were identified with the Sentieon pipeline. Variants were annotated and filtered to identify potentially pathogenic mutations. Candidate variants were validated by Sanger sequencing. The *FUS* c.1574C>T (p.P525L) mutation was validated using the following primers: Forward: 5'-GAGGGCTAGGTGGAAAGACC-3'□ Reverse: 5'-GGTCACTTTTAATGGGAACCA-3'

Immunofluorescence Staining

Cells were plated on glass coverslips at 1 × 10^4 cells per well and cultured overnight. After fixation with 4% paraformaldehyde, permeabilization with 0.1% Triton X-100, and blocking with 5% BSA in PBS, the cells were incubated overnight at 4 °C with anti-FUS (Proteintech, 11570-1-AP) and anti-mitochondria (Abcam, ab92825) primary antibodies. After washing, fluorescent secondary antibodies were applied for 1 h at room temperature in the dark. Nuclei were counterstained with DAPI, and coverslips were mounted with DAPI-containing antifade medium.

Mitochondrial and Total DNA Extraction

Mitochondria were isolated using the Mitochondrial Isolation and Protein Extraction Kit following the manufacturer's instructions. In brief, 2 × 10^7 cells were harvested, washed with ice-cold PBS, resuspended in Mitochondrial Isolation Reagent A, homogenized on ice with a Dounce homogenizer, and fractionated by differential centrifugation. The mitochondrial pellet was subsequently used for mtDNA extraction with the TIANamp Genomic DNA Kit, and DNA quality was assessed by NanoDrop spectrophotometry.

For total genomic DNA extraction used in mtDNA copy number analysis, cells were lysed directly without prior mitochondrial isolation, and DNA was extracted with the same kit following the manufacturer's protocol. DNA concentration and purity were then determined by NanoDrop spectrophotometry.

Quantification of mtDNA Copy Number and mtG4DNA Content

Total genomic DNA was used as the template for mtDNA copy number analysis, with COX3 as the mtDNA-specific target and GAPDH as the reference gene. All samples were analyzed in triplicate, and relative mtDNA copy number was calculated using the ΔΔCt method and normalized to the control group. To determine mtG4DNA content, DNA extracted from isolated mitochondria was used as the template. qPCR was conducted using primers targeting a G4-enriched region within the CYTB gene, and normalized to a non-G4 region within ND1. The ΔCt method was applied to assess the relative abundance of G4-prone mtDNA. Primer sequences were listed in Table S7.

ATP Level Quantification

Intracellular ATP was quantified using a luminescence-based assay kit following the manufacturer's protocol. 1 × 10^6 cells were lysed in 200 µL lysis buffer, and 10 µL of the post-centrifugation supernatant was combined with 90 µL working solution in a 96-well plate for immediate luminescence measurement. ATP levels were calculated from a standard curve and normalized to cell number (nmol/10^6 cells).

Mitochondrial Bioenergetic Profiling

C2C12, MCF-10A, and COS-7 cells (3 × 10^4 cells/well) as well as primary skin fibroblasts from patients and healthy controls (1.5 × 10^4 cells/well) were seeded in Seahorse XFe24 microplates and allowed to attach overnight. Mitochondrial respiration was evaluated using the Seahorse Mito Stress Test, with sequential injection of oligomycin (1 µM), FCCP (1 µM), rotenone (0.5 µM), and antimycin A (0.5 µM). Basal respiration, ATP production, maximal respiration, and spare respiratory capacity were analyzed in Seahorse XF Base Medium containing 10 mM glucose, 1 mM pyruvate, and 2 mM glutamine (pH 7.4), and results were normalized to cell number.

Ethics Statement

This study was approved by the Medical Ethics Committee of Qilu Hospital of Shandong University (approval number: 2020066). Written informed consent was obtained from all participants prior to enrollment. All procedures were conducted in accordance with the Declaration of Helsinki and relevant ethical guidelines.

Statistical Analyses

Statistical analyses were performed using SPSS software (version 21.0; IBM Corp., Armonk, NY, USA). One-way ANOVA was used for comparisons among multiple groups. The Student's *t-test* was applied for pairwise comparisons. Data are expressed as mean ± SD ($n = 3$). *$p < 0.05$, **$p < 0.01$, ***$p < 0.001$.

Declarations

Acknowledgements

This work was supported by the National Natural Science Foundation of China (52373190, K.N.W.; 22307064, K.N.W. and 82203050, Y.X.), the Natural Science Foundation of Shandong Province, China (ZR2023QB144, K.N.W.), the Special Fund of Taishan Scholars Project of Shandong Province, China (tsqn202306032 K.N.W.), the Shenzhen Science and Technology Research and Development Funds, China (JCYJ20230807094115031, K.N.W.; and JCYJ20240813101224032, K.N.W.), and the Qilu Young Scholars Program of Shandong University, and the National Research Foundation of Korea (2018R1A3B1052702, J.S.K.; RS-2023-00241100, Y.X.).

We gratefully acknowledge Professor Stephen Tait from the University of Glasgow, Glasgow, UK, for his selfless guidance in the experiments and manuscript writing.

Author Contributions

K.N.W. and X.R.H. designed the research. X.R.H., Y.L., and K.N.W. are responsible for all phases of the research. M.D.C. and M.Z. helped with the synthesis of SDMNA and imaging. E.K. and J.K. participated in the data analysis. F.L., J.K., Z.L., X.Y., J.S.K., and C.Y. provided reagents and samples. X.R.H. and Y.L. wrote the manuscript. Y.X., K.N.W., and X.R.H. reviewed and edited the manuscript. K.N.W. supervised the study.

Competing interests

The authors declare no competing interests.

References

1. Nass MM. Mitochondrial DNA: Advances, Problems, and Goals. *Science* **165**, 25-35 (1969).
2. Pandith A., Luo Y., Jang Y., Bae J., Kim Y. Self-Assembled Peptidyl Aggregates for the Fluorogenic Recognition of Mitochondrial DNA G-Quadruplexes. *Angew Chem. Int. Ed.* **62**, e202215049 (2023).
3. Liu H., Zhuang H., Feng D. Quality control of mitochondrial nucleoids. *Trends Cell Biol.* **35**, 922-932 (2025).
4. Petros JA*., et al.* mtDNA mutations increase tumorigenicity in prostate cancer. *Proc. Natl. Acad. Sci. U.S.A.* **102**, 719-724 (2005).
5. Kopinski PK., Singh LN., Zhang SP., Lott MT., Wallace DC. Mitochondrial DNA variation and cancer. *Nat. Rev. Cancer* **21**, 431-445 (2021).
6. Phillips AF*., et al.* Single-Molecule Analysis of mtDNA Replication Uncovers the Basis of the Common Deletion. *Mol. Cell* **65**, 527-538. (2017).
7. Newman LE*., et al.* Mitochondrial DNA replication stress triggers a pro-inflammatory endosomal pathway of nucleoid disposal. *Nat. Cell Biol.* **26**, 194-206 (2024).
8. Fang EF., Scheibye-Knudsen M., Chua KF., Mattson MP., Croteau DL., Bohr VA. Nuclear DNA damage signalling to mitochondria in ageing. *Nat. Rev. Mol. Cell Biol.* **17**, 308-321 (2016).
9. Vielhaber S*., et al.* Mitochondrial DNA abnormalities in skeletal muscle of patients with sporadic amyotrophic lateral sclerosis. *Brain* **123**, 1339-1348 (2000).
10. Goutman SA*., et al.* Emerging insights into the complex genetics and pathophysiology of amyotrophic lateral sclerosis. *Lancet Neurol.* **21**, 465-479 (2022).
11. Feldman EL*., et al.* Amyotrophic lateral sclerosis. *Lancet* **400**, 1363-1380 (2022).
12. Huang R*., et al.* Unprecedented enantio-selective live-cell mitochondrial DNA super-resolution imaging and photo-sensitizing by the chiral ruthenium polypyridyl DNA "light-switch". *Nucleic Acids Res.* **51**, 11981-11998 (2023).
13. Doimo M*., et al.* Enhanced mitochondrial G-quadruplex formation impedes replication fork progression leading to mtDNA loss in human cells. *Nucleic Acids Res.* **51**, 7392-7408 (2023).

14. Sprenger HG*., et al.* Cellular pyrimidine imbalance triggers mitochondrial DNA-dependent innate immunity. *Nat. Metab.* **3**, 636-650 (2021).
15. Wang Y., Guo X., Ye K., Orth M., Gu Z. Accelerated expansion of pathogenic mitochondrial DNA heteroplasmies in Huntington's disease. *Proc. Natl. Acad. Sci. U.S.A.* **118**, e2014610118 (2021).
16. Ishiguro A., Lu J., Ozawa D., Nagai Y., Ishihama A. ALS-linked FUS mutations dysregulate G-quadruplex-dependent liquid-liquid phase separation and liquid-to-solid transition. *J. Biol. Chem.* **297**, 101284 (2021).
17. Chen X-C*., et al.* Monitoring and Modulating mtDNA G-Quadruplex Dynamics Reveal Its Close Relationship to Cell Glycolysis. *J. Am. Chem. Soc.* **143**, 20779-20791 (2021).
18. Blom H., Widengren J. Stimulated Emission Depletion Microscopy. *Chem. Rev.* **117**, 7377-7427 (2017).
19. Vicidomini G., Bianchini P., Diaspro A. STED super-resolved microscopy. *Nat. Methods* **15**, 173-182 (2018).
20. Xu JQ*., et al.* Ultrastructural visualization of chromatin in cancer pathogenesis using a simple small-molecule fluorescent probe. *Sci. Adv.* **8**, eabm8293 (2022).
21. Torrado B., Pannunzio B., Malacrida L., Digman MA. Fluorescence lifetime imaging microscopy. *Nat. Rev. Methods Primes* **4**, 80 (2024).
22. Tan Z*., et al.* Time-resolved fluorescent proteins expand fluorescent microscopy in temporal and spectral domains. *Cell* **188**, 6987-7005 (2025).
23. Summers PA*., et al.* Visualising G-quadruplex DNA dynamics in live cells by fluorescence lifetime imaging microscopy. *Nat. Commun.* **12**, 162 (2021).
24. Ma JB*., et al.* Chemical Control of Fluorescence Lifetime towards Multiplexing Imaging. *Angew Chem. Int. Ed.* **63**, e202403029 (2024).
25. Minoshima M., Reja SI., Hashimoto R., Iijima K., Kikuchi K. Hybrid Small-Molecule/Protein Fluorescent Probes. *Chem. Rev.* **124**, 6198-6270 (2024).
26. Chan J, Dodani SC., Chang CJ. Reaction-based small-molecule fluorescent probes for chemoselective bioimaging. *Nat. Chem.* **4**, 973-984 (2012).
27. Zhai R*., et al.* Small-molecule fluorogenic probes for mitochondrial nanoscale imaging. *Chem. Soc. Rev.* **52**, 942-972 (2023).
28. Ko K., Gao M., Sarkar S., Kwon H-Y., Chang Y-T. Oxaborole-Functionalized Sialylated Glycan Probe for High-Fidelity Fluorescence Imaging of Cancer Tissue. *J. Am. Chem. Soc.* **147**, 19718-19726 (2025).
29. Wang X., Qin G., Yang J., Zhao C., Ren J., Qu X. A subcellular selective APEX2-based proximity labeling used for identifying mitochondrial G-quadruplex DNA binding proteins. *Nucleic Acids Res.* **53**, gkae1259 (2025).
30. Qin J*., et al.* ER-mitochondria contacts promote mtDNA nucleoids active transportation via mitochondrial dynamic tubulation. *Nat. Commun.* **11**, 4471 (2020).

31. Stadler C.*, et al.* Immunofluorescence and fluorescent-protein tagging show high correlation for protein localization in mammalian cells. *Nat. Methods* **10**, 315-323 (2013).
32. Ozawa T., Natori Y., Sato M., Umezawa Y. Imaging dynamics of endogenous mitochondrial RNA in single living cells. *Nat. Methods* **4**, 413-419 (2007).
33. Dua N., Seshadri A., Badrinarayanan A. DarT-mediated mtDNA damage induces dynamic reorganization and selective segregation of mitochondria. *J. Cell Biol.* **221**, e202205104 (2022).
34. Zhang SB.*, et al.* PicoGreen Assay of Circular DNA for Radiation Biodosimetry. *Radiat Res.* **183**, 188-195 (2015).
35. Anal BiochemTuma RS.*, et al.* Characterization of SYBR Gold nucleic acid gel stain: a dye optimized for use with 300-nm ultraviolet transilluminators. *Anal. Biochem.* **268**, 278-288 (1999).
36. Wu J.*, et al.* Dipyridylphenylamine-based chemodosimeter for sulfite with optimizing ratiometric signals via synchronous fluorescence spectroscopy. *Dyes and Pigments* **136**, 175-181 (2017).
37. Liu LY.*, et al.* Quantitative Detection of G-Quadruplex DNA in Live Cells Based on Photon Counts and Complex Structure Discrimination. *Angew Chem. Int. Ed.* **59**, 9719-9726 (2020).
38. Pandith A., Luo Y., Jang Y., Bae J., Kim Y. Self-Assembled Peptidyl Aggregates for the Fluorogenic Recognition of Mitochondrial DNA G-Quadruplexes. *Angew Chem. Int. Ed.* **62**, e202215049 (2022).
39. Huang WC.*, et al.* Direct evidence of mitochondrial G-quadruplex DNA by using fluorescent anti-cancer agents. *Nucleic Acids Res.* **43**, 10102-10113 (2015).
40. Liu T.*, et al.* Multi-color live-cell STED nanoscopy of mitochondria with a gentle inner membrane stain. *Proc. Natl. Acad. Sci. U.S.A.* **119**, e2215799119 (2022).
41. Wojtaszek JL.*, et al.* Structure-specific roles for PolG2-DNA complexes in maintenance and replication of mitochondrial DNA. *Nucleic Acids Res.* **51**, 9716-9732 (2023).
42. Lin Q.*, et al.* A lipid droplet-targeted probe for imaging of lipid metabolism disorders during mitochondrial myopathy. *Talanta* **292**, 127901 (2025).
43. Iwashita H.*, et al.* Small fluorescent molecules for monitoring autophagic flux. *FEBS Letters* **592**, 559-567 (2018).
44. Chen Q.*, et al.* Fast, three-dimensional, live-cell super-resolution imaging with multiplane structured illumination microscopy. *Nat. Photonics* **19**, 567-576 (2025).
45. Demmerle J.*, et al.* Strategic and practical guidelines for successful structured illumination microscopy. *Nat. Protoc.* **12**, 988-1010 (2017).
46. Kujoth GC.*, et al.* Mitochondrial DNA mutations, oxidative stress, and apoptosis in mammalian aging. *Science* **309**, 481-484 (2005).
47. Huang HH.*, et al.* Reversible compromise of physiological resilience by accumulation of heteroplasmic mtDNA mutations. *Science* **390**, 164-172 (2025).
48. Beers DR., Appel SH. Immune dysregulation in amyotrophic lateral sclerosis: mechanisms and emerging therapies. *Lancet Neurol.* **18**, 211-220 (2019).

49. Sephton CF*., et al.* Activity-dependent FUS dysregulation disrupts synaptic homeostasis. *Proc. Natl. Acad. Sci. U.S.A.* **111**, E4769-4778 (2014).
50. Kodavati M*., et al.* FUS unveiled in mitochondrial DNA repair and targeted ligase-1 expression rescues repair-defects in FUS-linked motor neuron disease. *Nat. Commun.* **15**, 2156 (2024).
51. Sharma A*., et al.* ALS-associated mutant FUS induces selective motor neuron degeneration through toxic gain of function. *Nat. Commun.* **7**, 10465 (2016).
52. Yu M*., et al.* Widespread Mislocalization of FUS Is Associated With Mitochondrial Abnormalities in Skeletal Muscle in Amyotrophic Lateral Sclerosis With FUS Mutations. *J. Neuropathol Exp. Neurol.* **81**, 172-181 (2022).
53. Deng J*., et al.* FUS Interacts with HSP60 to Promote Mitochondrial Damage. *PLoS Genet* **11**, e1005357 (2015).
54. Vummidi BR., Alzeer J., Luedtke NW. Fluorescent probes for G-quadruplex structures. *Chem. Bio. Chem.* **14**, 540-558 (2013).
55. Dragan AI., Casas-Finet JR., Bishop ES., Strouse RJ., Schenerman MA., Geddes CD. Characterization of PicoGreen Interaction with dsDNA and the Origin of Its Fluorescence Enhancement upon Binding. *Biophys. J.* **99**, 3010-3019 (2010).
56. Biffi G., Tannahill D., McCafferty J., Balasubramanian S. Quantitative visualization of DNA G-quadruplex structures in human cells. *Nat. Chem.* **5**, 182-186 (2013).
57. Chen X-C*., et al.* Monitoring and Modulating mtDNA G-Quadruplex Dynamics Reveal Its Close Relationship to Cell Glycolysis. *J. Am. Chem. Soc.* **143**, 20779-20791 (2021).
58. Mohanty J., Barooah N., Dhamodharan V., Harikrishna S., Pradeepkumar PI., Bhasikuttan AC. Thioflavin T as an Efficient Inducer and Selective Fluorescent Sensor for the Human Telomeric G-Quadruplex DNA. *J. Am. Chem. Soc.* **135**, 367-376 (2013).
59. Xiong K*., et al.* Facilitating Quantitation of Mitochondrial G-Quadruplex DNA with an Iridium(III) Two-Photon Phosphorescence Lifetime Imaging Probe. *J. Am. Chem. Soc.* **147**, 47701-47711 (2025).
60. Frisch M*., et al.* Gaussian 09 (Revision D.01). (2009).
61. Bayly CI., Cieplak P., Cornell WD., Kollman PA. A Well-Behaved Electrostatic Potential Based Method Using Charge Restraints for Deriving Atomic Charges - the Resp Model. *J. Phys. Chem.* **97**, 10269-10280 (1993).
62. Morris GM*., et al.* AutoDock4 and AutoDockTools4: Automated Docking with Selective Receptor Flexibility. *J. Comput. Chem.* **30**, 2785-2791 (2009).
63. Morris GM*., et al.* Automated docking using a Lamarckian genetic algorithm and an empirical binding free energy function. *J. Comput. Chem.* **19**, 1639-1662 (1998).
64. Schrödinger LLC., DeLano W. PyMOL. 2.4.0 (2020).

Scheme 1

Scheme 1 is available in the Supplementary Files section.

Figures

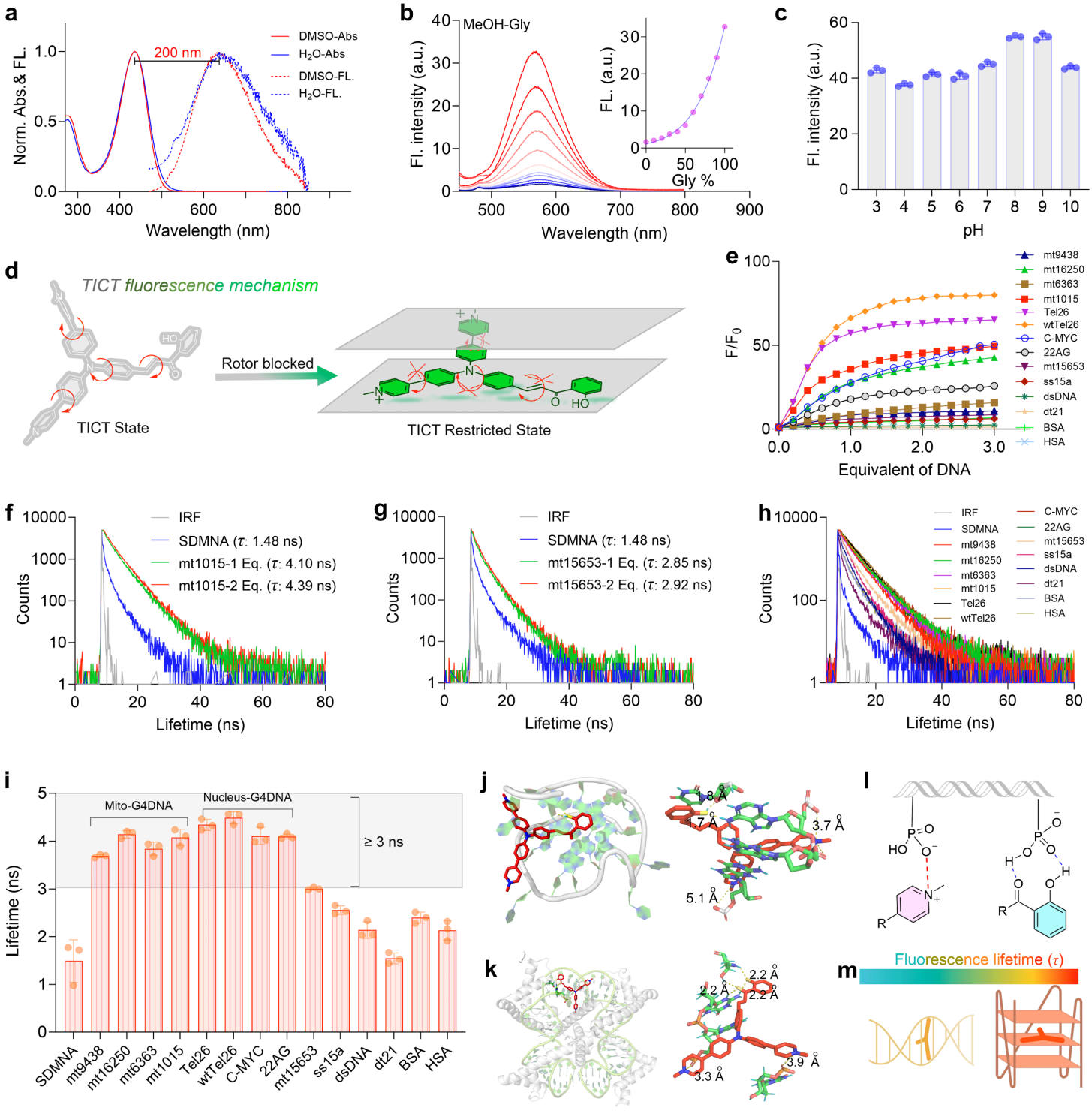


Figure 1

Photophysical properties of SDMNA and its topology-dependent response to DNA. (a) Normalized absorption and fluorescence emission spectra of SDMNA (5 μM) in DMSO and H_2O. (b) Fluorescence emission changes of SDMNA (5 μM) in MeOH/glycerol mixtures with varying viscosity. (c) Fluorescence intensity of SDMNA (5 μM) in Britton-Robinson (BR) buffer over a pH range of 3-10. (d) Schematic

illustration of fluorescence intensity enhancement and lifetime extension caused by TICT inhibition. (e) Relative fluorescence intensity changes of SDMNA (1 μM) upon titration with different G4DNA topologies, dsDNA topologies, and protein in 10 mM Tris-HCl buffer (pH 7.2, 100 mM K^+). λ_{ex} = 450 nm. (f, g) Fluorescence lifetime decay curves of SDMNA (1 μM) upon titration with different amounts of mtDNA1015 (f) and mtDNA15653 (g) in 10 mM Tris-HCl buffer (pH 7.4, 100 mM K^+). λ_{ex} = 445 nm, λ_{em} = 570 nm. (h, i) Representative fluorescence lifetime decay curve (h) and corresponding fluorescence lifetime value statistics (i) of SDMNA in the presence of DNA at a DNA: SDMNA ratio of 2: 1. λ_{ex} = 445 nm. (j) Molecular docking model of SDMNA bound to C-MYC (G4DNA) (PDB ID: 6jj0) with an enlarged view of the binding interface. (k) Molecular docking model illustrating the interaction of SDMNA with a mitochondrial DNA protein complex (PDB ID: 7lbw). (l) Schematic diagram of electrostatic and hydrogen bonding interactions between SDMNA and DNA. (m) Schematic diagram of fluorescence lifetime changes upon SDMNA binding to dsDNA and G4DNA.

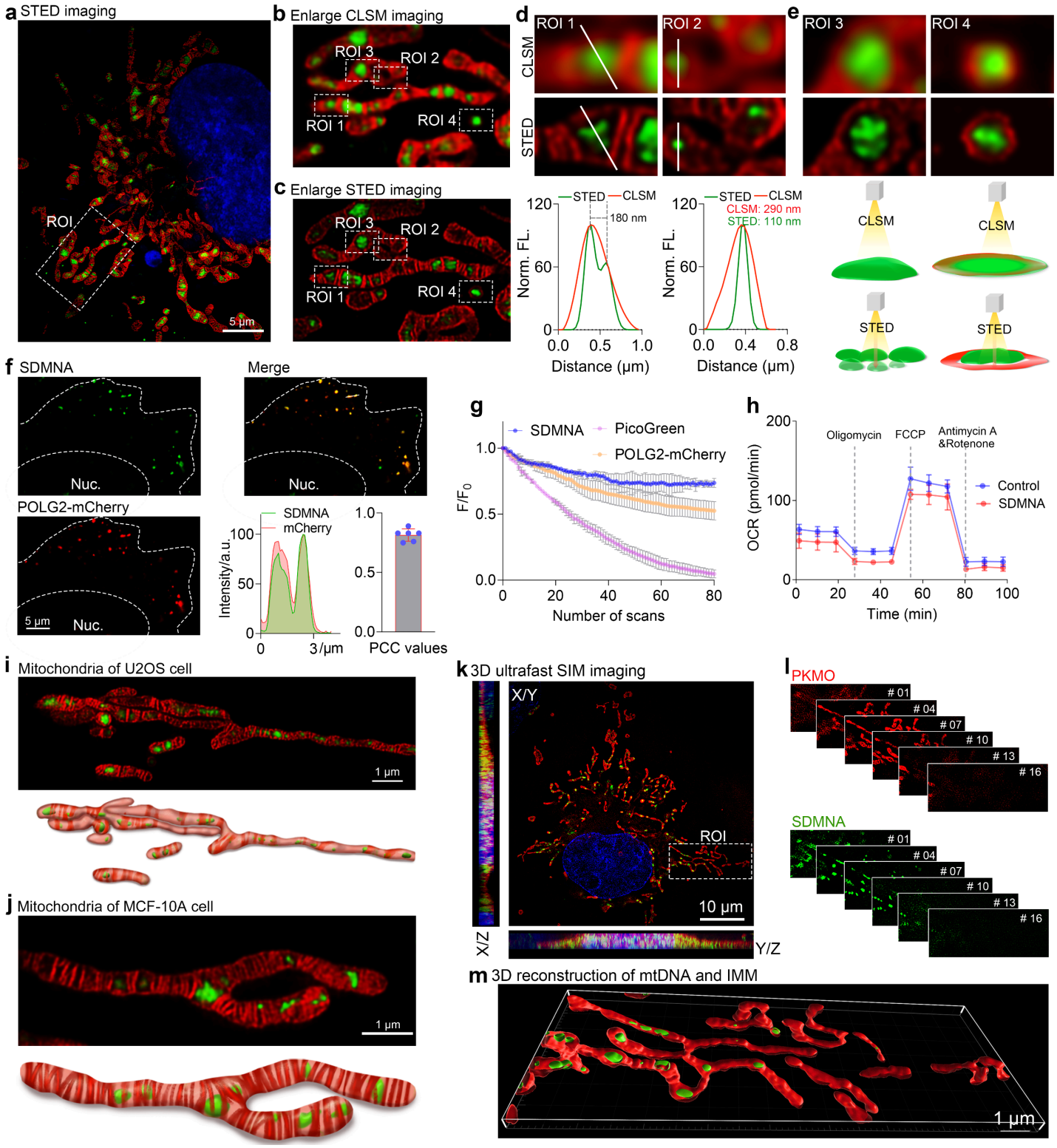


Figure 2

STED and SIM super-resolution imaging of mitochondrial nucleoids in living cells. (a) STED super-resolution image showing mtDNA and mitochondrial inner membrane in living COS-7 cells stained with SDMNA (green, 2 μM), PK Mito Orange (PKMO, red, 250 nM), and Hoechst 33342 (blue, 1 μg/mL). Scale bar: 5 μm. (b) Enlarged confocal laser scanning microscope (CLSM) image of the region outlined in (a). (c) Enlarged STED image of the same region shown in (a). (d) Enlarged STED view of the outlined region

in (c) and corresponding CLSM image. The line profile shows SDMNA normalized fluorescence intensity along the white dashed line. (e) EnlargedSTED and corresponding CLSM images of one of several DNA regions on a filamentous mitochondrion with internal DNA outlined in (c). The line profile shows SDMNA-normalized fluorescence intensity along the white dashed line. (f) Co-localization analysis of SDMNA and homo-POLG2-mCherry in living cells. Scale bar: 5 μm. (g) Photostability comparison showing changes in normalized fluorescence intensity of SDMNA, PicoGreen, and homo-POLG2-mCherry stained cells under continuous laser irradiation. (h) Seahorse analysis of mitochondrial respirationin COS-7 cells with or without SDMNA treatment (2 μM, 3 h). (i-j) STED imaging of mitochondrial morphology and mtDNA using PKMO and SDMNA, respectively, in U2OS (i) and MCF-10A (j). (k) 3D ultrafast SIM imaging of mtDNA within mitochondria in living COS-7 cells, reconstructed from consecutive Z-stack images with maximum fluorescence intensity projection. The cells were stained with SDMNA (green), MTDR (red), and Hoechst 33342 (blue). Scale bar: 10 μm. (l) Enlarged views of the region of interest (ROI) indicated by the white dashed box in (k). (m) 3D surface reconstruction of ROI shown in (k), generated using Imaris software.

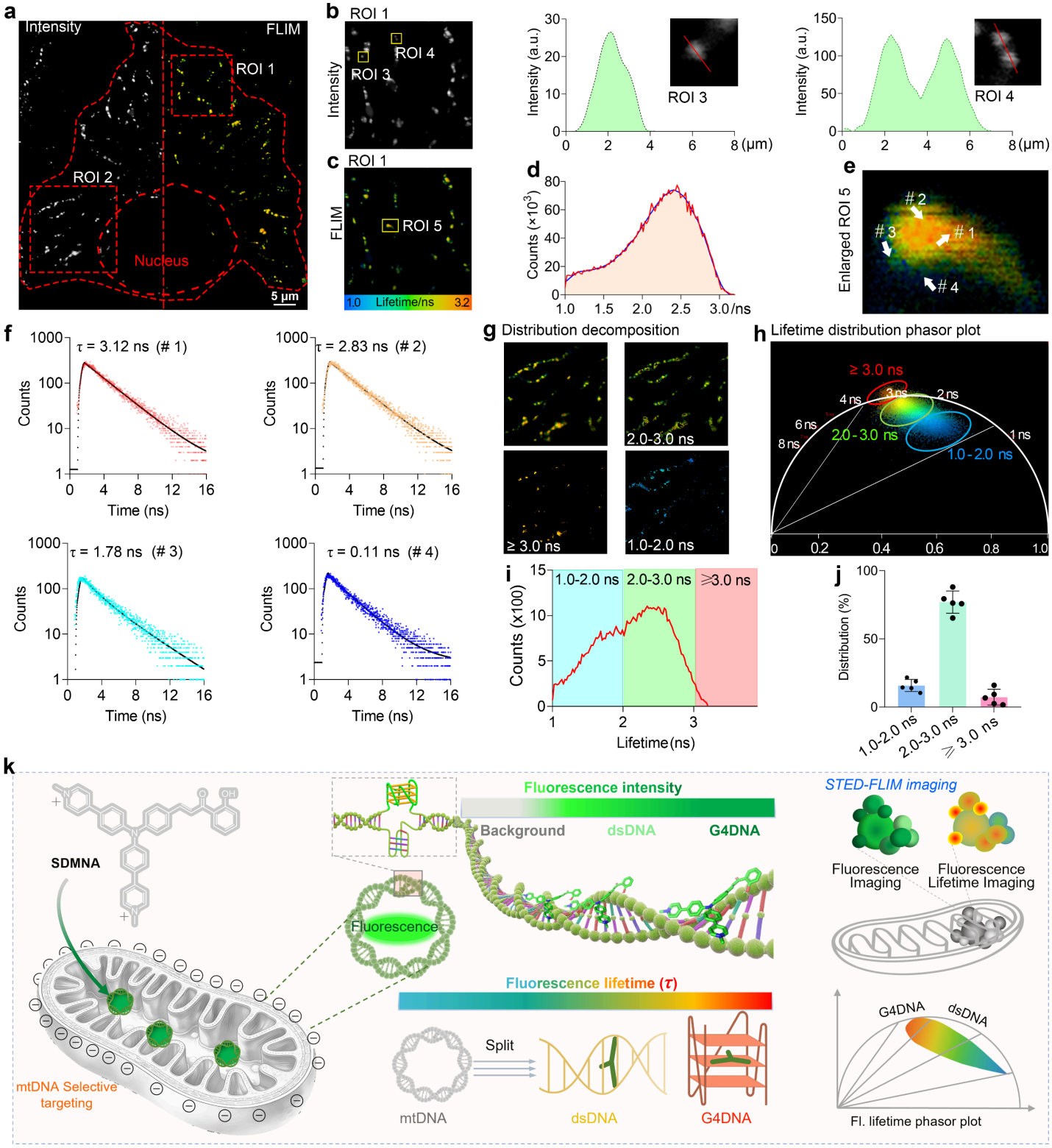


Figure 3

Fluorescence lifetime-resolved analysis of cellular mtDNA by SDMNA. (a) FLIM image of a living COS-7 cell incubated with SDMNA; white punctate features indicate regions of high fluorescence intensity. (b) Magnified view of ROI 1 from (a), showing the intensity map, and corresponding fluorescence intensity profile along the indicated red line. (c) Zoomed FLIM image of ROI 1. (d) Statistical distribution of fluorescence lifetimes extracted from the FLIM data in (c). (e) Enlarged FLIM image of a single

mitochondrial nucleoid (ROI 5) from (c). (f) Fluorescence lifetime decay curves corresponding to positions #1, #2, #3, and #4 are indicated in (e). (g-h) Decomposed fluorescence lifetime images of ROI 2 (g) and the corresponding phasor plots (h). (i) Statistical analysis of the fluorescence lifetime distribution in (g). (j) Quantification of photon counts within different fluorescence lifetime intervals. (k) Schematic illustration of SDMNA binding to mtDNA and generating topology-dependent fluorescence intensity/lifetime signals for real-time, *in-situ* STED/FLIM super-resolution analysis of mtDNA.

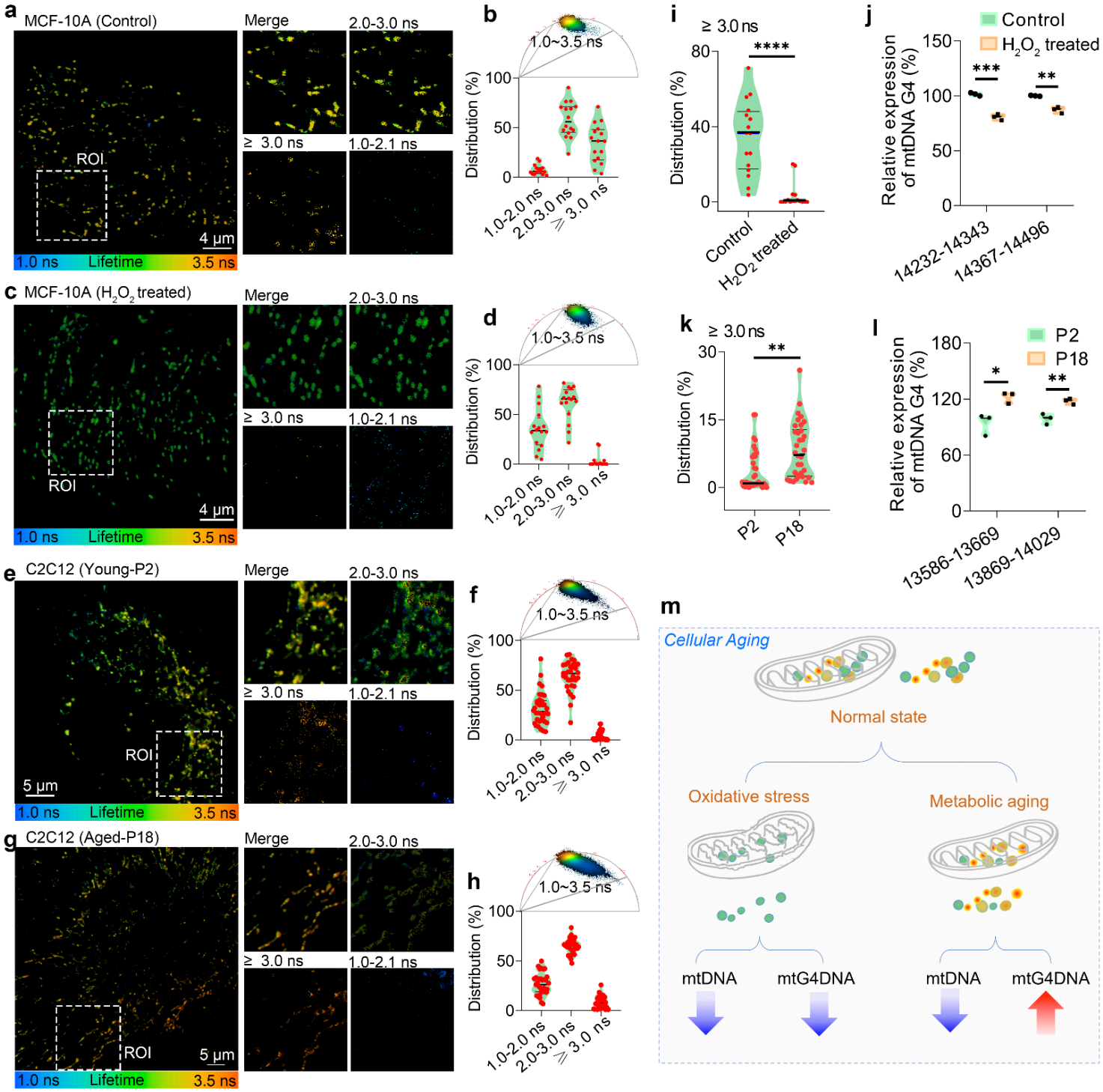


Figure 4

FLIM imaging and metabolic profiling reveal distinct mtG4DNA alterations under oxidative stress and replicative senescence. (a) FLIM images of normal MCF-10A cells and corresponding lifetime-segmented images of ROI. (b) Phasor plot corresponding to (a) and statistical distribution of fluorescence lifetimes across different lifetime intervals (n = 16). (c) FLIM images of H_2O_2-treated MCF-10A cells and corresponding lifetime-segmented images of ROI. (d) Phasor plot corresponding to (c) and statistical distribution of fluorescence lifetimes across different lifetime intervals (n = 16). (e) FLIM images of early-passage C2C12 cells (passage 2, P2) and corresponding lifetime decomposed images of ROI. (f) Phasor plot corresponding to (e) and statistical distribution of fluorescence lifetimes across different lifetime intervals (n = 34). (g) FLIM images of replicative senescent C2C12 cells (passage 18, P18) and corresponding fluorescence lifetime-segmented images of ROI. (h) Phasor plot corresponding to (g) and statistical distribution of fluorescence lifetimes across different lifetime intervals (n = 34). (i) Comparison of the ≥3 ns fluorescence lifetime populations between normal and H_2O_2-treated MCF-10A cells derived from (b) and (d). (j) Results obtained by qPCR of the copy number of G4 susceptible mtDNA region in normal and H_2O_2-treated MCF-10A cells. (k) Comparison of the ≥3.0 ns fluorescence lifetime populations between P2 and P18 C2C12 cells derived from (f) and (h). (l) Results obtained by qPCR of the copy number of the G4 susceptible mtDNA region in P2 and P18 C2C12 cells. (m) Schematic illustration summarizing SDMNA-enabled quantification of dsDNA and G4DNA within mitochondrial nucleoids during oxidative stress-induced senescence and replicative aging via high-resolution fluorescence lifetime profiling. Mean ± SD, n =3. *P < 0.05, **P < 0.01, ***P < 0.001.

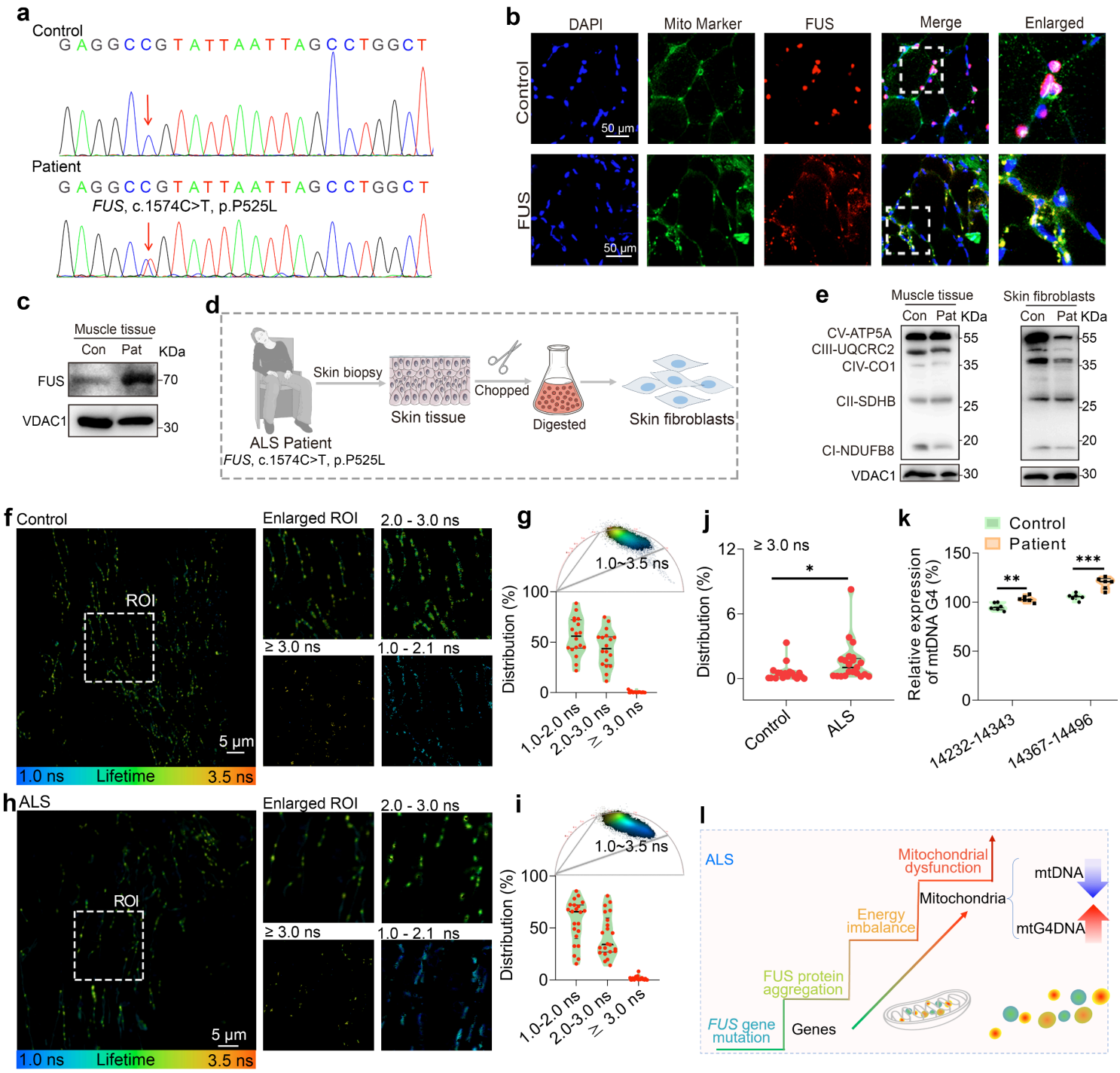


Figure 5

Mitochondrial G4DNA perturbation and mitochondrial dysfunction in ALS samples with *FUS*mutations. (a) Sanger sequencing confirmed the presence of the *FUS* c.1574C>T, p.P525L mutation in the patient's muscle tissue. (b) Immunofluorescence staining showed abnormal localization of mutant FUS (red) in patient muscle cells, co-stained with the mitochondrial marker HSP60 (green); nuclei were stained with DAPI (blue). (c) Western blot analysis demonstrates elevated expression of mutant FUS protein in patient muscle tissue. (d) Schematic workflow illustrating the derivation of patient fibroblasts from skin biopsy samples. (e) Western blot analysis showing reduced expression of mitochondrial electron transport chain complexes I-V in patient muscle and patient-derived fibroblasts. (f) FLIM images of healthy control

human skin fibroblast and corresponding lifetime-segmented images of ROI. (g) Phasor plot corresponding to (f) and statistical distribution of fluorescence lifetimes across different lifetime intervals (n = 18). (h) FLIM images of ALS patient-derived human skin fibroblast and corresponding lifetime-segmented images of ROI. (i) Phasor plot corresponding to (h) and statistical distribution of fluorescence lifetimes across different lifetime intervals (n = 21). (j) Comparison of the ≥3ns fluorescence lifetime populations between healthy control and ALS patient fibroblasts derived from (g) and (i). (k) Results obtained by qPCR of the copy number of the G4 susceptible mtDNA region in healthy control and ALS patient-derived fibroblasts. (l) Schematic illustration summarizing SDMNA-enabled quantification of dsDNA and G4DNA remodeling within mitochondrial nucleoids during ALS progression via high-resolution fluorescence lifetime profiling. Mean ± SD, n = 3. *P < 0.05, **P < 0.01, ***P < 0.001.

Supplementary Files

This is a list of supplementary files associated with this preprint. Click to download.

- ESINat.Commun.260325final.docx.pdf
- MovieS1.avi
- Scheme1.png